



The effects of warm pre-stressing on cleavage fracture. Part 2: finite element analysis

D.J. Smith ^{a,*}, S. Hadidimoud ^a, H. Fowler ^b

^a Department of Mechanical Engineering, University of Bristol, Queen's Building, University Walk, Bristol BS8 1TR, UK

^b Frazer-Nash Consultancy Limited, Bristol BS51 5TE, UK

Received 12 November 2002; received in revised form 22 August 2003; accepted 30 September 2003

Abstract

Finite element analyses have been performed to simulate and verify the findings of the extensive experimental programme aimed to characterise the mechanical parameters and the cleavage fracture response following warm pre-stressing of two steels, BS1501 and A533B as detailed in part 1 [The Effects of Warm Pre-Stressing on Cleavage Fracture. Part 1: Evaluation of Experiments, companion paper]. A stress matching approach to predicting the fracture response of the as received, as well as the warm pre-stressed specimens is suggested. Using the stress distributions from the finite element analyses prediction of fracture after WPS is examined and results are compared to the experimental data and those obtained by combining the Chell [Int. J. Fract. 17 (1) (1981) 61; Proc. 4th Int. Conf. Pres. Ves. Technol., 1980, p. 117; Int. J. Pres. Ves. Pip. 23 (1986) 121] WPS model with the Wallin [Defect Assessment in Components, Fundamentals and Applications,ESIS/EGF 9, Mechanical Engineering Publications, London, 1991, p. 415] failure probability model described in part 1 [The Effects of Warm Pre-Stressing on Cleavage Fracture. Part 1: Evaluation of Experiments, companion paper]. The significance of residual stress field in enhancing of cleavage fracture toughness following warm pre-stressing has been highlighted. Using the appropriate finite element models, the role of sub-critical crack growth and crack tip blunting are also investigated.

© 2003 Elsevier Ltd. All rights reserved.

Keywords: WPS; Stress matching; Finite element; Cleavage fracture; Residual stress

1. Introduction

Many engineering components are subjected to “proof” loading prior to service operation. This “proof” loading is often used to demonstrate the integrity of a finished product. One feature of proof loading that has gained recognition is the benefit that may be obtained in improving in-service component reliability particularly when the component is operated at a temperature lower than the proof load. This type of “proof” loading and subsequent low temperature operation is often called warm pre-stressing. This feature is important when considering a component containing postulated defects.

* Corresponding author. Tel.: +44-117-928-8212; fax: +44-117-929-4423.

E-mail address: david.smith@bristol.ac.uk (D.J. Smith).

Nomenclature

E	Young modulus, MPa
K, K_I	mode-I stress intensity factor, MPa $\sqrt{\text{m}}$
K_f	toughness at fracture (experimental), MPa $\sqrt{\text{m}}$
K_{Ic}	mode-I fracture toughness (theoretical), MPa $\sqrt{\text{m}}$
K_1	pre-load stress intensity factor, MPa $\sqrt{\text{m}}$
J_e	the elastic J -integral, N/m
a	crack length, mm
W	specimen ligament, mm
B	specimen thickness, mm
r	distance from the crack tip, mm
r_c	characteristic distance ahead of the crack tip, mm
R	extent of plastic zone, mm
R_1, R_2, R_3	extent of plastic zones on pre-load, unload and reload respectively, mm
n	power law hardening exponent
m, q	functions of the hardening exponent n
$u(a)$	displacement at tip, mm
$u(x)$	displacement at distance x from tip, mm
L_{blunt}	normalised matching distance for blunted tip
L_{sharp}	normalised matching distance for sharp tip
L_{HRR}	normalised matching distance for HRR model
σ_Y	the material yield stress, MPa
σ_{yy}	stress component normal to the crack plane, MPa
σ_c	characteristic stress at distance r_c , MPa
σ_R	proof load reference stress, MPa
σ_{Rf}	reference stress at fracture, MPa
σ_{Rc}	reference critical stress, MPa
σ_{Y1}	yield point at proof load temperature, MPa
σ_{Y2}	yield point at fracture temperature, MPa
σ_{YC}	yield point in compression, MPa
σ_{mt}	pre-load maximum tensile stress, MPa
ξ	non-dimensional parameter
$\sigma_0, \alpha, \epsilon_0$	material constants in Ramberg–Osgood power law relationship
$\tilde{\sigma}_{yy}$	non-dimensional constant, MPa
I_n	a function of hardening exponent n

There are many different temperature-loading paths to be considered for the component. In laboratory based experimental work three main pre-stressing, cooling and unloading cycles have been studied named as LCF, LCUF and LUCF, where L is pre-load, U is unload, C is cool and F is reload to fracture. Smith and Garwood [6,7] summarised a wide range of experimental results from earlier studies for these different cycles. The LCF cycle provides the largest improvement in toughness with the minimum benefit from warm pre-stressing occurring for the LUCF cycle [8].

In companion paper [1] we examined more recent experimental evidence for the effects of warm pre-stressing on low temperature cleavage fracture of two ferritic steels. The results were collated from labo-

ratory based research using the LUCF cycle. It was demonstrated that warm pre-stressing at a temperature on the upper shelf generally increased the low temperature fracture load compared to the fracture load without warm pre-stressing. The results were compared with an analytical model developed by Chell and co-workers [2–4]. Notably we introduced the Chell model into a simple probabilistic analysis [5] to demonstrate how warm pre-stressing changed failure probability. Without recourse to a probabilistic analysis there arises uncertainty in the interpretation of the results. For example, earlier studies show general agreement with the predicted trends, but often there was considerable scatter in the results.

Surprisingly, while the basic analytical models were developed over twenty years ago there have been no supporting numerical studies to verify or otherwise study these theories. Nonetheless finite element (FE) work has been carried out to examine, for example, the application of the "local approach" to warm pre-stressing [9]. Recent numerical studies considered scatter in fracture toughness using probabilistic models. For example, Stöckl et al. [10] and Kordish et al. [11] incorporated modified probabilistic models developed by the Beremin group [9] to predict cleavage fracture following WPS. Stöckl et al. [10] also compared simulations with experimental results. Their results were used to suggest that crack tip blunting is the main feature that provides the improved cleavage toughness following WPS. Valeta et al. [12] used results obtained from a 2-D finite element analysis in conjunction with the Beremin model to demonstrate the WPS effect on fracture toughness and compared the predictions with the Chell model. To validate their approach they used the experimental fracture test results of two independent test programmes carried out to study the load history effects on cleavage toughness of the same reactor pressure vessel steel. Using probabilistic fracture mechanics computer codes Yagawa et al. [13] performed sensitivity analyses to evaluate the influence of a range of parameters including WPS on failure probability. Their study suggested that WPS significantly affected the failure probability of the nuclear reactor pressure vessels subjected to pressurised thermal shock. According to Lidbury et al. [14] results of NESC-1 PTS benchmark experiments indicate that scatter in material toughness, the most significant uncertainty factor influencing the integrity assessment, arises from a range of structural features including residual stresses, constraint and WPS effect. They suggest that 3-D FE simulations can be used to estimate the local constraint parameters for specific specimen geometries related to the fracture test data.

Recently Chen et al. [15] argued that a primary parameter in enhancement of apparent toughness following WPS is reduction in normal tensile stress due to decrease of the stress triaxiality and strain developing in front of the blunted tip. It was also argued that residual compressive stresses play a secondary role. Their study of the mechanism of WPS effects on toughness includes FE analyses of various WPS cycles to determine the normal stress, triaxiality and plastic strain distributions around the crack tip modelled with slight blunting.

In this paper we focus on results obtained from elastic–plastic finite element studies to assess the validity of the analytical models developed for LUCF warm pre-stressing. In Section 2 we summarise the relevant analytical models. Essential ingredients for the FE studies are the tensile elastic–plastic properties of the steel. Experiments were carried out to determine these properties and results are described in Section 3. The FE studies are described in Section 4, where predictions of near crack tip residual stresses are provided first. This is followed by the description of a method for determining the effects of warm pre-stressing from the FE analyses. The method is applied to a stationary crack and then to an extended crack. Finally in Section 5 our results are assessed in light of the experimental results reported in the companion paper.

2. Analytical models

Two models developed by Chell [2] and Curry [16] remain the main methods for predicting the effects of warm pre-stressing. A detailed review of the models is given by Smith and Garwood [6]. In each model it is essential to determine the relative sizes of the crack tip plastic zones following each loading step. For

example, if the plastic zone at the low temperature fracture load is larger than the plastic zones created by pre-loading and unloading the models predict that there is no benefit obtained from warm pre-stressing. Conversely if the fracture plastic zone is within the former plastic zones the near crack tip stresses, strains and displacements are a function of the prior load history. The two models use different underlying assumptions. Curry's model, extended by Smith and Garwood [7,17,18], uses stress superposition. Chell used discrete yielding and displacement superposition to determine the effects of load and temperature history. Here we will summarise only the essential features of these models to provide a foundation for the subsequent FE analyses.

2.1. Displacement superposition model

To predict the effect of warm pre-stressing on lower shelf cleavage fracture Chell and co-workers [2–4] proposed a failure criterion that describes fracture when plastic and residual stress zones occur. The criterion uses the J -integral (J_e) that contains only elastic components. This criterion is used, together with a model for strip yielding [19], to determine the conditions for onset of failure for different loading paths. For example, for a contour shrunk on to the yielded region the integral J_e is given by:

$$J_e = K_{Ic}^2/E = \sigma_{Y2}\{u(a) - u(x)\} \quad (1)$$

where $u(a)$ and $u(x)$ are displacements at the crack tip and at a point x across the yielded region, E is Young's modulus and K_{Ic} is the fracture toughness for small scale yielding conditions.

In the model for strip yielding the displacements u for small scale yielding are given by:

$$u(x) = \frac{K_I^2}{\sigma_Y E} f(x/R) \quad (2)$$

where σ_Y is the yield stress and the function $f(x/R)$ is:

$$f(x/R) = \left\{ \xi - \frac{x}{2R} \ln \left(\frac{1+\xi}{1-\xi} \right) \right\} \quad (3)$$

and

$$\xi = \left(1 - \frac{x}{R} \right)^{1/2} \quad (4)$$

where R is the extent of the plastic zone, given by:

$$R = \frac{\pi K_I^2}{8 \sigma_Y^2} \quad (5)$$

Using Eqs. (1)–(5), Chell demonstrated that for LUCF conditions the failure stress intensity factor K_f is obtained from:

$$\frac{K_{Ic}^2}{\sigma_{Y2}} = \frac{K_{Ic}^2}{\sigma_{Y1}} \left\{ 1 - f\left(\frac{R_3}{R_1}\right) \right\} - \frac{K_I^2}{2\sigma_{Y1}} \left\{ 1 - f\left(\frac{R_3}{R_2}\right) \right\} + \frac{K_f^2}{(\sigma_{Y1} + \sigma_{Y2})} \quad (6)$$

where σ_{Y1} and σ_{Y2} are the yield stresses at the proof load and fracture load temperatures respectively. The ratios R_3/R_1 and R_3/R_2 are given by:

$$\frac{R_3}{R_2} = \left(\frac{K_f}{K_I} \right)^2 \left(\frac{2\sigma_{Y1}}{\sigma_{Y2} + \sigma_{Y1}} \right)^2 \quad (7)$$

and

$$\frac{R_3}{R_1} = \left(\frac{K_f}{K_1}\right)^2 \left(\frac{\sigma_{Y1}}{\sigma_{Y2} + \sigma_{Y1}}\right)^2 \quad (8)$$

Eq. (6) is relevant only to the “LUCF” case in which the final fracture plastic zone is smaller than the prior load and unloaded plastic zones. The solution to Eq. (6) requires a numerical method. An approximate analytical method is provided by Chell [4]. Since the focus of this paper is the LUCF warm pre-stressing the analytical solutions for other temperature-load paths are not discussed here.

2.2. Stress superposition models

Curry [16] proposed an alternative method for predicting the effect of warm pre-stressing on lower shelf cleavage fracture. Curry’s model is based on plastic superposition of stresses and uses the Ritchie, Knott and Rice (RKR) fracture criterion [20]. The critical stress intensity factor, K_{Ic} , is proportional to the product $\sigma_c \sqrt{r_c}$, where σ_c is a characteristic stress and r_c is a characteristic distance ahead of the crack tip. Solutions for different temperature-load paths can be determined. For the LUCF case with a final fracture plastic zone smaller than prior load and unload plastic zones, the stress distribution at fracture is given by the superposition of the pre-load–unload–reload stages as follows:

$$\sigma_{yy}[K_f] = \sigma_{yy}[K_1, \sigma_{Y1}] - \sigma_{yy}[K_1, 2\sigma_{Y1}] + \sigma_{yy}[K_1, (\sigma_{Y1} + \sigma_{Y2})] \quad (9)$$

where σ_{yy} is the stress component normal to the crack plane. For each loading condition this stress is a function of the current stress intensity factor and the yield stress. Curry [16] suggested using finite element stress distributions from one load case to infer the stress σ_{yy} for the other load cases. Smith and Garwood [7,17] sought an analytical solution using the Hutchinson, Rice and Rosengren (HRR) stress field [21,22] for a power law hardening material. Using Eq. (9) as a starting point the ratio of the fracture toughness after WPS, K_f , to the as-received toughness is given by:

$$\frac{K_f}{K_{Ic}} = \left(\frac{\sigma_{Y1}}{\sigma_{Y2}}\right)^{m/q} \left\{ 1 - \left(\frac{\sigma_{Y1}}{\sigma_{Y2}}\right)^m \left(\frac{K_1}{K_{Ic}}\right)^q (1 - 2^m) \right\}^{1/q} \quad (10)$$

where $m = (n - 1)/(n + 1)$ and $q = 2(n + 1)$ with n the power law hardening exponent.

Unlike the Chell and Curry’s models, that are based on the local crack tip stress/strain distributions, Smith and Garwood [7] also proposed using a “reference stress” in the net section (or un-cracked ligament) of the component. This provides an approximate description of the global behaviour that leads to differences between pre-stressed and non-pre-stressed components. The reference stress approach simply modifies the analytical solution (Eq. (10)) obtained by Smith and Garwood [7] for the model proposed by Curry [16], by replacing the toughness ratio by the reference stress ratio as:

$$\frac{\sigma_{Rf}}{\sigma_{Rc}} = \left(\frac{\sigma_{Y1}}{\sigma_{Y2}}\right)^{m/q} \left\{ 1 - \left(\frac{\sigma_{Y1}}{\sigma_{Y2}}\right)^m \left(\frac{\sigma_R}{\sigma_{Rc}}\right)^q (1 - 2^m) \right\}^{1/q} \quad (11)$$

Here the proof load reference stress, σ_R , and the reference stress at fracture, σ_{Rf} , are by definition limited to the yield stresses at the pre-load and the fracture temperatures respectively.

Since the Chell, Curry and Smith and Garwood models can be expressed in terms of the ratios of stress intensity factors, K_f/K_{Ic} and K_1/K_{Ic} predictions are shown in Fig. 1. To determine the curves shown in Fig. 1 it was assumed that σ_{Y1} is 530 MPa and σ_{Y2} is 818 MPa for A533B steel at 20 and -170 °C respectively. Also shown are the experimental results from two earlier studies by Reed and Knott [23–25] and Loss et al. [26]. Note that in each of these experimental studies the average K_{Ic} at the fracture temperature quoted by each researcher is used to determine the ratios K_f/K_{Ic} and K_1/K_{Ic} .

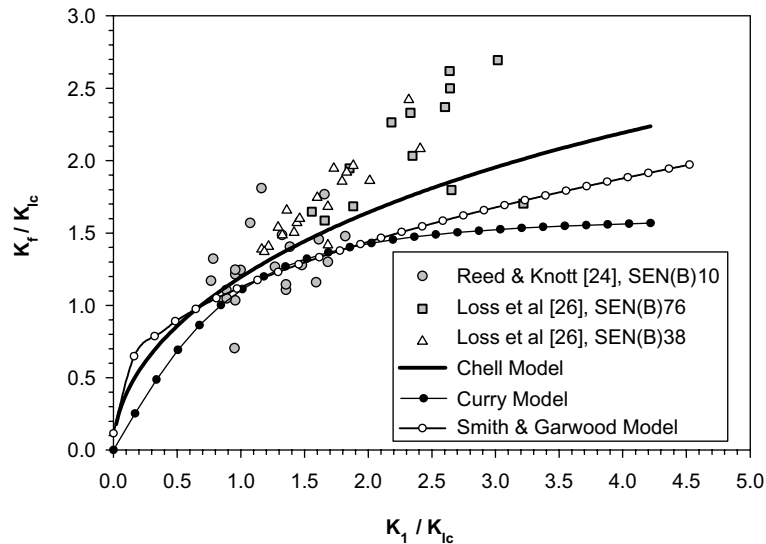


Fig. 1. Comparison between experimental data and theoretical predictions of WPS effect for A533B steel following an overload (K_1) at 20 °C.

Overall at low pre-load levels the agreement between the experiments and mode I predictions is good. However at high pre-load levels the models tend to underestimate the WPS effect from the LUCF loading cycle. Later in the paper we will focus on comparing the Chell model with FE simulations.

3. Tensile stress–strain behaviour

Prior to the FE simulations it was essential to explore the material's stress–strain behaviour. The tensile stress–strain response will be affected if the component is subjected to significant levels of the prior loading history resulting in “localised” plastic deformation. This effect is related to the hardening behaviour of the material. Interpretation of results using finite element analysis will therefore require taking account of the material deformation plasticity on overloading and unloading throughout the loading history. The experiments carried out to determine these properties for both candidate steels and the interpretation for isotropic and kinematic hardening responses are explained in this section.

Previous experimental investigations [18,26–28], performed to characterise the mechanical and fracture response of BS1501 and A533B steels, included uni-axial studies to obtain material data for finite element modelling. For BS1501 steel the upper and lower yield point were a distinct feature observed in its response. The yield stress of this steel increased as the temperature was reduced. The steel exhibited an almost perfectly plastic stress–strain response after yielding at different test temperatures. Following unloading to zero strain and then reloading under strain control the strong upper and lower yielding behaviour exhibited earlier was not repeated. The perfectly plastic material response was retained at low temperature although at room temperature some hardening was observed following loading and unloading cycles.

Under cyclic loading the yielding response in tension and compression was observed to vary. Following the initial tensile load, the sharp upper and lower yield points were not reproduced when loaded in compression. These observations are summarised in Fig. 2 where curves for various loading conditions applied to BS1501 steel at 20 and –120 °C. Similar results are obtained if the material is pre-stressed at 20 °C and fractured at –70 °C.

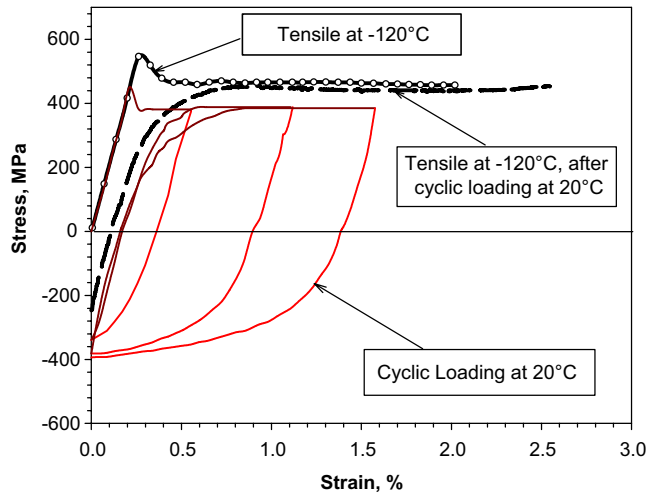


Fig. 2. Deformation response of BS1501 steel for different loading histories.

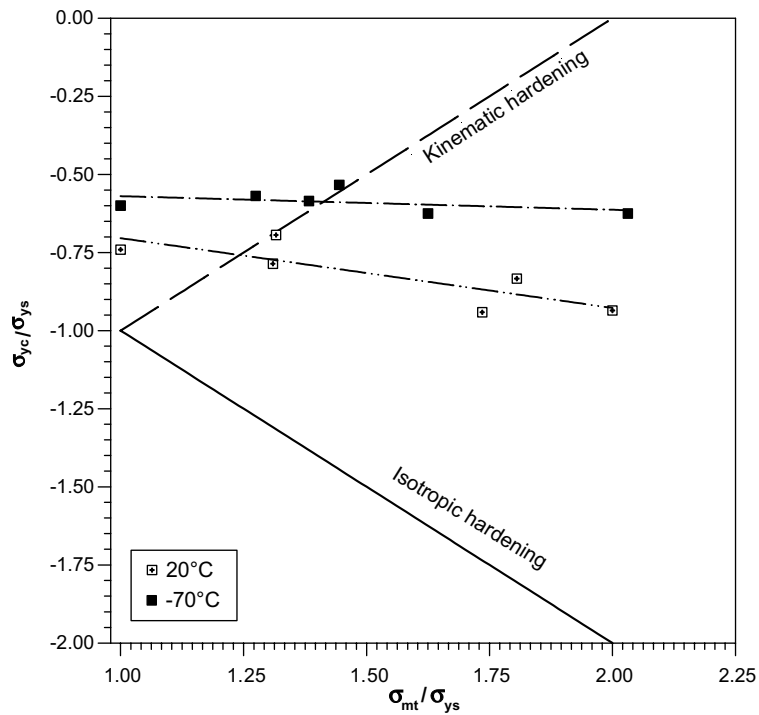


Fig. 3. Influence of prior plastic deformation on subsequent compressive yielding behaviour of BS1501 steel.

It is evident from the results in Fig. 2 that the steel does not exhibit simple isotropic or kinematic hardening behaviour when subjected to pre-loading. For example, Fig. 3 shows the experimental results for the yield stress in compression (σ_{yc}), following pre-stressing at σ_{mt} in tension for tests at 20 and -70 °C.

Tests at $-120\text{ }^{\circ}\text{C}$ show similar results. Also shown are the predicted changes in compressive yield stress assuming isotropic and kinematic hardening. It is apparent that after moderate levels of pre-stressing, the material response is bounded by the isotropic and kinematic hardening models.

The response of A533B Class 1 steel has been characterised also in previous studies [6,17,18,28]. This steel tested at two temperatures (20 and $-170\text{ }^{\circ}\text{C}$) exhibits broadly similar yielding behaviour to that of BS1501 steel, with sharp upper and lower yielding behaviour observed at both temperatures. But, it was noticeable that at both temperatures the material hardens following yielding. Garwood and Smith [18] and Fowler [28] also investigated the influence of prior plastic deformation on subsequent yielding in compression for this steel. The influence of prior tensile loading was very similar to that shown in Fig. 3 for BS1501 steel.

Rather than attempting to model the complex material behaviour shown in Figs. 2 and 3 it was decided to use both isotropic and kinematic hardening laws in the FE simulations. Furthermore the upper and lower yielding response was ignored and the true stress–true strain data at each appropriate temperature were used directly in the FE analysis.

4. Finite element studies

The results of numerical simulations of the effects of warm pre-stress load histories on the candidate steels are presented in this section. The ABAQUS-CAE (version 6.2) [29] finite element code was used throughout the study. Elastic–plastic finite element studies were performed to provide an insight into the crack tip stress fields during the warm pre-stress cycle and at fracture. The FE models analysed include two-dimensional models of SEN(B) and C(T) with appropriate mesh refinement at the crack tip area to obtain consistent results. Experimental results for these specimen configurations are explained in part 1 [1]. Plane strain analyses were carried out using both isotropic and kinematic hardening laws with the ratio of crack length to the crack width, a/W , equal to 0.5. The results from the FE simulations are first presented in terms of the residual stresses generated after unloading following pre-loading. A method of predicting fracture following warm pre-stress in the FE simulations is then presented for both sharp and blunted cracks. This is followed by results of simulations for crack extension after pre-loading.

4.1. Residual stresses

The first step in the FE analysis was to examine the residual stresses developed after pre-loading and unloading. This loading cycle was applied to the SEN(B) specimen using a sharp-tip crack with $a/W = 0.5$ and $W = 25\text{ mm}$ and assuming small deformation behaviour. A series of analyses were carried out with the pre-load corresponding to the a stress intensity factor of $K = 97\text{ MPa}\sqrt{\text{m}}$, and assuming plane stress, plane strain, isotropic and kinematic hardening conditions.

The results from various analyses are shown in Fig. 4. The residual stress generated after unloading is strongly dependent on the material model and stress state. For a given stress state (e.g. plane stress) the peak near tip residual stress for kinematic hardening was approximately one half that for isotropic hardening. Further away from the crack tip (at distances greater than about 2 mm) the residual stresses were similar irrespective of the hardening model. Although not shown in Fig. 4, when residual stress fields from different pre-loads are compared, the peak residual stress is the same and the region of compressive residual stress increases with increasing pre-load. Finite element results for pre-load and unload simulations for the C(T) specimen yielded very similar results for the residual stress distributions near to the crack tip.

Earlier results from experimental measurements [6,7], using neutron diffraction method on a 25 mm thick SEN(B) specimen with $(W - a) = 25\text{ mm}$ are also shown in Fig. 4. For distances $r/(W - a)$ greater than 0.12 from the crack tip there is good agreement between measurements and predictions. However

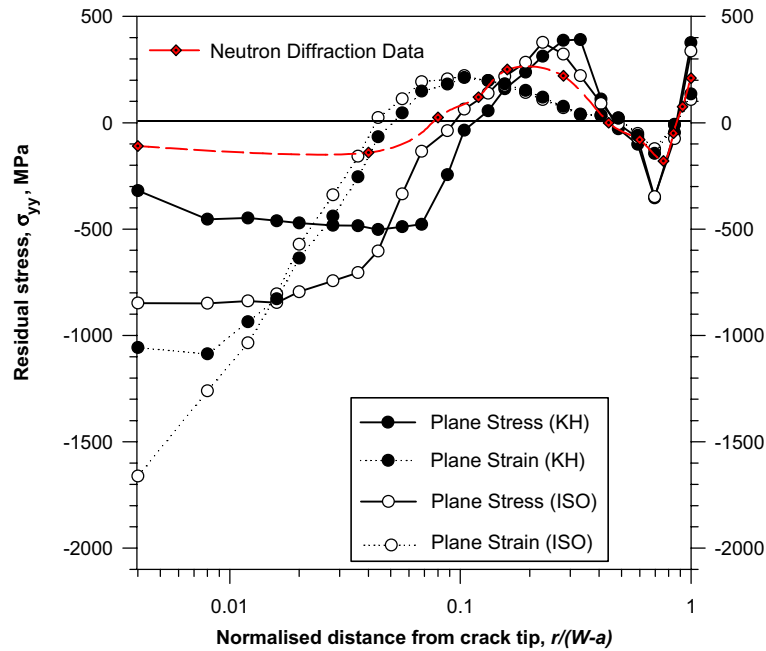


Fig. 4. Distribution of normal to the crack plane residual stresses for plane stress and plane strain conditions for SEN(B) with $a/W = 0.5$ and $(W - a) = 25$ mm (KH = kinematic hardening, ISO = isotropic hardening).

close to the crack tip it is evident that the magnitude of the measured residual stresses are substantially smaller than predicted from the FE analyses.

4.2. Prediction of fracture after WPS

The load cases used to provide input to the FE analyses following unloading were developed from the experimental studies of Smith and Garwood [18] and Fowler [28]. Finite element simulations for these experiments were carried out for both BS1501 and A533B steels. For BS1501 steel the fracture temperatures were -120 and -70 °C and for A533B steel the fracture temperatures were -170 and -100 °C. The results for both steels were broadly similar for a variety of loading conditions. As with the residual stress predictions, simulations were carried out for both the SEN(B) and C(T) geometry. Here attention is confined to the SEN(B) specimen with $a/W = 0.5$ and $(W - a) = 50$ mm using A533B material properties. Finite element simulations of fracture were performed for two experimental load histories called the as-received (AR) and LUCF conditions. The as-received condition is when there is no pre-loading (or warm pre-stressing) prior to loading to brittle fracture. The fracture temperature used in the simulations was -170 °C, with the corresponding tensile stress–strain behaviour at this temperature obtained from the experiments described earlier. The LUCF load history corresponds to pre-loading and unloading at room temperature followed by cooling and reloading to fracture at -170 °C. The analyses simulating the LUCF cycle were performed in three discrete steps. Initially the specimen was loaded to the maximum experimental applied load at room temperature. It was then incrementally unloaded to zero load at the same temperature. Finally the specimen was cooled down to the fracture temperature and reloaded to fracture. The analyses were performed using both the isotropic and kinematic hardening laws.

Finite element analyses were carried out first for sharp-tipped cracks and small displacements. Later simulations were conducted for a blunt crack and assuming large displacements. As with the analyses for the residual stresses these subsequent loading analyses were carried out for isotropic and kinematic hardening conditions.

4.2.1. Sharp cracks

Initially in the FE simulations fracture after WPS was predicted using the RKR [20] model and linking the model to the HRR field as suggested by the Curry [16] and Smith and Garwood [7] models described earlier. The maximum principal stress near to the crack tip for a non-linear elastic material, based on the Ramberg–Osgood power law relationship, is given by:

$$\sigma_{yy} = \sigma_0 \left(\frac{J}{\alpha \varepsilon_0 I_n \sigma_0 r} \right)^{1/n+1} \tilde{\sigma}_{yy}[\theta, n] \quad (12)$$

where σ_0 , α and ε_0 are material constants and $\tilde{\sigma}_{yy}$ is a non-dimensional constant. I_n was determined for plane strain conditions from:

$$I_n = 10.3 \sqrt{0.13 + \frac{1}{n} - \frac{4.6}{n}} \quad (13)$$

A typical HRR maximum principal stress distribution corresponding to a fracture load in the as-received state and determined from Eq. (12) is shown in Fig. 5. The J -integral in Eq. (12) was determined directly from the ABAQUS FE analysis. Also shown is the stress distribution corresponding to the as-received fracture condition obtained from the FE analysis. Both the HRR and FE stress distributions correspond to a sharp tip crack and small displacements. For $r/(W - a) < 0.002$ there is excellent agreement between the HRR and FE stress distributions.

Also shown in Fig. 5 are stress distributions for the LUCF simulations. The residual stress distribution generated by proof loading to $K = 63.2 \text{ MPa } \sqrt{\text{m}}$ and unloading is shown in Fig. 5 for isotropic and kinematic hardening. Tensile and compressive residual stresses were confined to distances less than $r/(W - a) = 0.4$, unlike the case for SEN(B) geometry with a pre-load $K = 97 \text{ MPa } \sqrt{\text{m}}$ shown in Fig. 4. As with the residual stress distributions shown in Fig. 4, results in Fig. 5 illustrate similar differences between isotropic and kinematic hardening near to the crack tip with the isotropic hardening model generating very high compressive residual stresses close to the crack tip.

In the LUCF cycle, on reloading at the lower temperature after unloading, it was found that the differences in the maximum principal stress distribution for kinematic and isotropic hardening became small and the stress distributions essentially the same at sufficiently higher loads. The stress distributions for the two hardening models for an intermediate loading at $K = 40.6 \text{ MPa } \sqrt{\text{m}}$, and at the fracture load with $K_f = 66 \text{ MPa } \sqrt{\text{m}}$ are shown in Fig. 5. In each load case the differences between the hardening models are small.

At different levels of reloading between $K = 40.6 \text{ MPa } \sqrt{\text{m}}$ and $K_f = 66 \text{ MPa } \sqrt{\text{m}}$ the FE results were assessed to determine the applicability of the RKR model to the LUCF cycle. It was found that the reloading and as-received stress distributions could be matched for distances $r/(W - a) < 0.002$ for a range of stress intensity factors between 50 and 66 $\text{MPa } \sqrt{\text{m}}$. In contrast, the stress distribution after WPS, that matched the as-received case, for distances as far as possible ahead of the crack tip, corresponded to a fracture load that was close to the experimental conditions. The matched stress distributions for kinematic and an isotropic hardening conditions are shown in Fig. 5. These results suggest that predictions of the WPS effects can be made using the stress superposition models at a limited distance ahead of the crack tip. However the results are ambiguous since there are many solutions between $K = 50$ and 60 $\text{MPa } \sqrt{\text{m}}$. Alternatively, when complete stress matching is made between the as-received and WPS maximum prin-

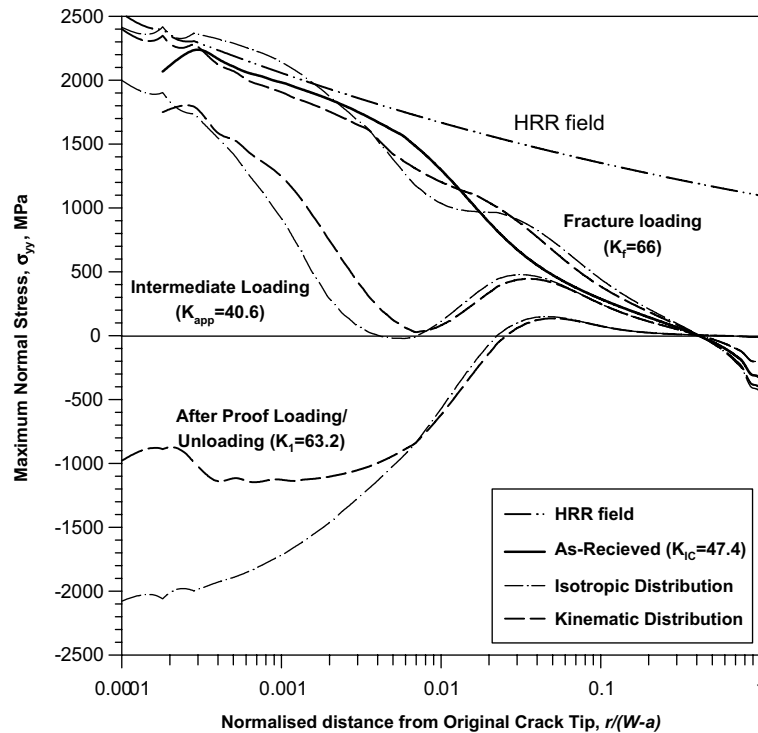


Fig. 5. Comparison of stress distributions in the crack tip region for isotropic and kinematic hardening materials for SEN(B) with $a/W = 0.5$, and $(W - a) = 50$ mm.

cipal stresses, the resulting fracture load following WPS is well defined. Based on the simulated stress fields for the as-received and warm pre-stressed conditions it was possible for the cleavage fracture toughness of a component to be predicted by matching the stress field formed on reloading to the stress field corresponding to the material's critical stress intensity factor. Many finite element analyses were then performed to examine this further by first simulating pre-loading events of different magnitudes at room temperature, unloading to zero load and reloading incrementally at low temperature. At each reload increment, the crack tip stress field was compared to the stress field corresponding to the as-received cleavage fracture toughness. Predictions of the critical stress intensity factor at maximum load were made using the load achieved at the increment where the stress distributions were in best agreement with the stress field for the as-received toughness.

The results of these FE predictions are summarised in Fig. 6, where the reloading maximum load fracture toughness determined by stress matching with as-received stress fields is shown as a function of the proof load K_1 . The results correspond to the fracture behaviour of A533B steel at -170 °C. Results are shown for four levels of fracture toughness that encompass the scatter in fracture toughness described in part 1 [1] for A533B at -170 °C. Also shown are predictions using the Curry [16] and Chell [2–4] models described earlier. For clarity the results of the Curry model are shown only for an as-received toughness of 47.4 MPa $\sqrt{\text{m}}$ and similar trends occur between the Chell and Curry models for higher levels of as-received toughness. Overall the FE analysis and the Chell model predict a larger increase in toughness than the Curry model for all levels of pre-load. This is similar to the results shown in Fig. 1. The FE predictions based on stress matching generally agree with the Chell model predictions at low levels of pre-load. At

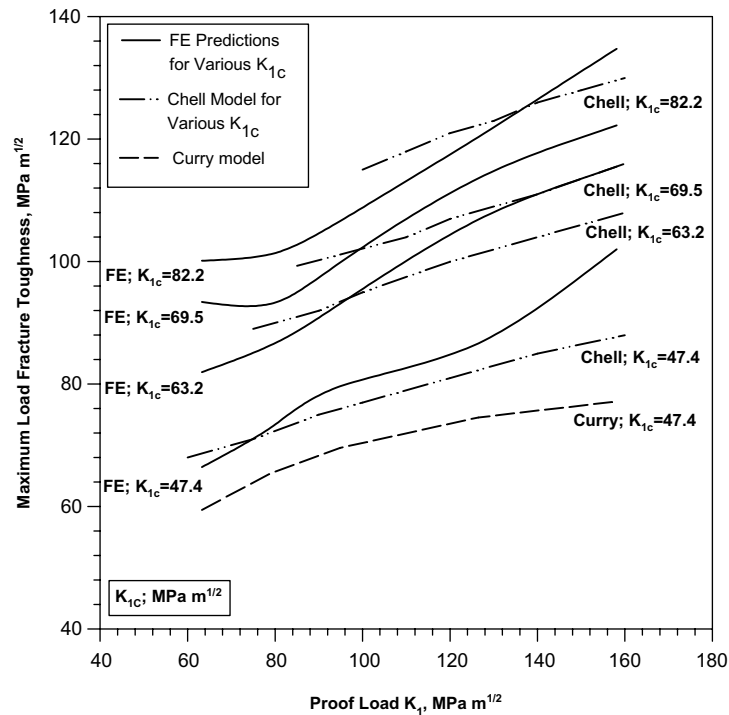


Fig. 6. Comparison between the WPS effect predictions from FE analysis and Chell and Curry models for A533B steel for pre-load at 20 °C and fracture at -170 °C.

higher pre-loads in the LUCF cycle the FE analysis provides a larger increase in maximum load toughness compared with the analytical models. The pre-load K_1 was determined from maximum load. An alternative approach is to estimate the pre-load J -integral and convert this to K_1 . This may result in better agreement with the Chell model at higher pre-loads.

4.2.2. Blunt cracks

The previous analyses for sharp cracks were repeated for an SEN(B) specimen containing an initially blunt crack with a root radius of 0.1 mm. The FE analysis was conducted assuming large displacements. The residual stress field distributions for the blunted and sharp crack configurations following unloading from the pre-load at room temperature are compared in Fig. 7. The residual stress distributions differ only between the sharp and blunt cracks close to the crack tip. The extent of the compressive region from the crack tip was essentially identical to the sharp crack. Therefore, crack tip blunting and large deformation theory only have an influence on the very near crack tip stress distribution during and following a pre-load event.

Predictions for the stress field at fracture for a blunt notched SEN(B) specimen in the as-received condition are shown in Fig. 7. The influence of warm pre-stress on the cleavage toughness of blunt notched specimen was then investigated. The specimen was pre-loaded at room temperature to 63.2 MPa \sqrt{m} and unloaded to zero load. The specimen was then cooled down to -170 °C and reloaded at this temperature until the stress field was matched, using the incremental loading technique described earlier. It was found that the blunt notch as-received and warm pre-stressed fracture stress fields matched for distances $L_{\text{blunt}} = r/(W - a)$ up to 0.006 from the crack tip. The matching distance, L_{blunt} , for the blunted case was

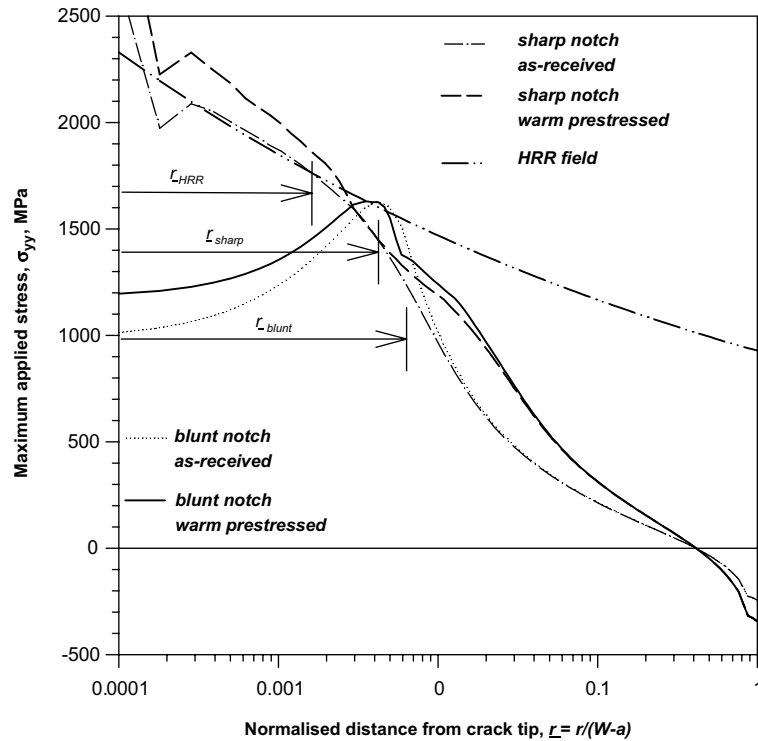


Fig. 7. Effect of blunting on crack tip stress compared with sharp cracks.

observed to be greater than the case of sharp notch (L_{sharp}). Once again the distance over which stresses were matched exceeds the distance over which the HRR field matches the stress distribution (L_{HRR}) as shown in Fig. 7. Consequently for both sharp and blunt cracked specimens, the stress field would need to be matched beyond the region of applicability of the HRR expression, Eq. (13).

Finally the stress matching method for the blunt cracks provided predictions following the LUCF cycle of the maximum load fracture toughness, K_{f1} , very similar to the results shown in Fig. 6 for the sharp crack analyses.

4.3. Effects of crack growth after WPS

The companion experimental work described in part 1 [1] examined the effects of subsequent crack extension following the pre-load cycle. Similar to the earlier analyses finite element simulations investigated using the stress-matching method to predict fracture following a warm pre-stress event and crack extension in C(T) specimens with $B = 25$ mm and $W = 50$ mm with an initial $a/W = 0.5$. The simulations were performed assuming kinematic hardening and in three discrete steps as before. However, the boundary conditions of the model were varied throughout the analysis. The simulation of crack extension was achieved by releasing nodal constraint in the plane ahead of the crack tip, up to the required distance in front of the crack. The crack extension was performed at zero load and therefore in the presence of compressive residual stresses. It was necessary to constrain the new free surfaces from crossing the plane of symmetry, while still being free to displace away from the symmetry plane. This was achieved by the introduction of contact surfaces on the crack plane. It was assumed that the contact elements on the crack

plane simulated a rigid surface. This surface was termed the master surface. The nodes of the elements in the crack plane of the original mesh were used to define the slave surface, which was considered as deformable. The master–slave surface contact formulation implemented within ABAQUS does not allow penetration of the master surface by the slave surface.

As additional non-linearity was introduced to the problem, severe discontinuity iterations were performed within the finite element code to calculate the distance between the integration points of the deformable and rigid surface elements. If this distance was positive, then there was no contact. If the distance was zero, then contact occurred and the normal pressure between the deformable and rigid surface was transmitted. Frictional effects between the contact surfaces were neglected in these analyses. Small strain theory was implemented throughout the analyses although the original crack tip was modelled using a finite radius of 0.05 mm.

A matrix of different toughness and crack extension combinations were examined. The as-received toughness levels of 40, 60 and 85 MPa $\sqrt{\text{m}}$ were representative of the range of experimental toughness. A proof load of 120 MPa $\sqrt{\text{m}}$ at room temperature and crack extensions of up to 4 mm from the crack tip prior to reloading at -170°C were used. The stress distributions at fracture and at -170°C were matched to fracture stress distributions for specimens in the as-received condition and for a notch tip radius of 0.05 mm. This was done for different amounts of crack extension. Typical results using the stress matching method are shown in Fig. 8. The maximum principal stress distribution corresponding to the as-received toughness is shown. This is the toughness for an extended crack of 1 mm (or when $r/(W-a) = 0.04$). Proof loading to $K = 120 \text{ MPa } \sqrt{\text{m}}$ and unloading introduced a residual stress field similar to that shown in Fig. 5. Nodal release to simulate 1 mm crack growth (i.e. $r/(W-a) = 0.04$) was then carried out. Since this

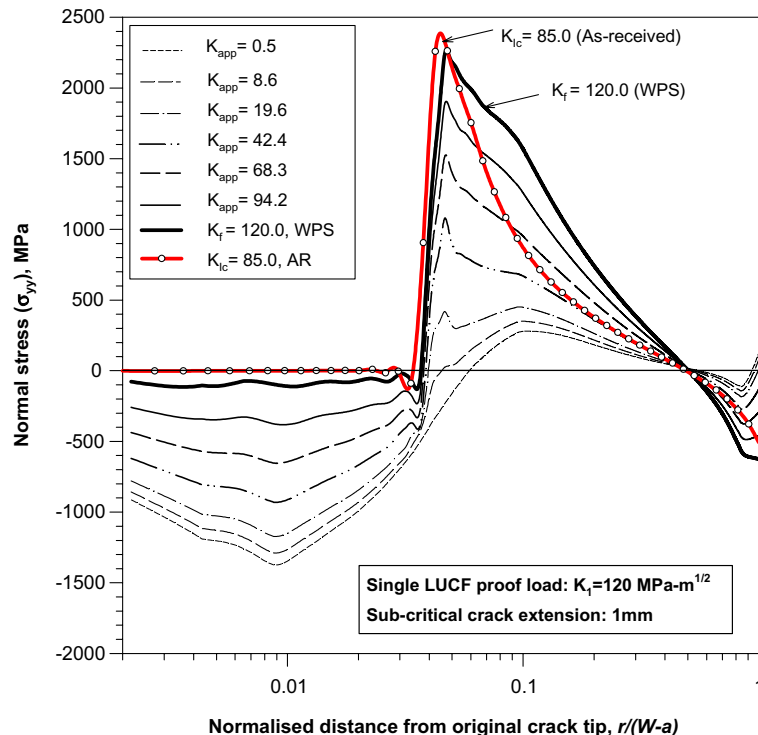


Fig. 8. Distribution of normal stress following warm pre-stressing and fracture following sub-critical crack growth.

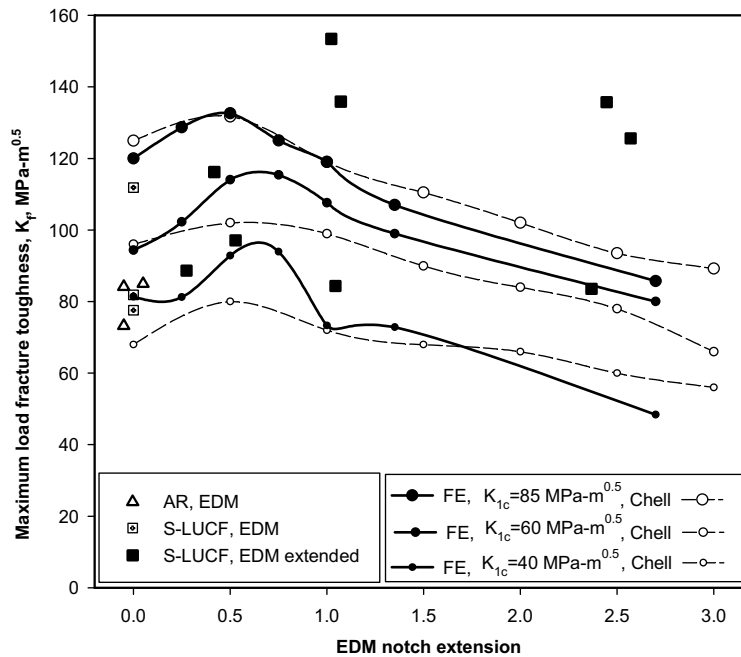


Fig. 9. Comparison of FE and Chell model predictions with the experimental results for sub-critical crack growth after proof loading (A533B steel C(T) specimens at -170 °C).

crack extension was within the compressive residual stress field the crack faces transmitted these stresses and did not perturb the residual stress distribution generated from warm pre-stressing. After cooling and then unloading the stress distribution directly ahead of the original crack tip changed as shown in Fig. 8. Unlike the earlier FE analyses, here the extent of stress matching was very limited. For example at $K_f = 120$ MPa \sqrt{m} after WPS stress matching occurred only near to the maximum of the as-received stress distribution.

Crack extension of 2.57 mm extended the crack into a region of tensile residual stress. It was observed that the stress distributions matched very close to the peak stress. The peak stress was found to reduce with increasing crack extension.

Fig. 9 illustrates the predictions for maximum load toughness, K_f as a function of crack growth increment and as-received cleavage toughness. The FE results compare extremely well with a model provided by Chell [2–4] that is an extension of the earlier model so that crack extension is introduced.

5. Discussion

The results of the finite element analyses have revealed a number of important features about the effects of warm pre-stressing on cleavage fracture. The predicted increase in toughness after WPS are not startlingly different from those developed by a number of theoretical models. However, the FE results have allowed us to examine a number of the underlying assumptions used in the analytical models. These assumptions are examined in more detail in the first part of the discussion. Later in the discussion the experimental data presented in part 1 [1] is re-examined in the light of the findings from the finite element studies.

5.1. Comparison of FE analysis with analytical models

Throughout the FE analysis it was assumed that fracture of the as-received material was associated with the maximum principal stress distribution in the plane normal to the crack and directly ahead of the crack. In the RKR fracture model [20], fracture takes place when a critical stress, σ_c is achieved at a characteristic (or critical) distance, r_c , ahead of the crack tip. In other words a single point on the maximum principal stress distribution is chosen. For the two steels studied here typical distances for r_c are about 150 μm [28]. In Figs. 5 and 6 this corresponds to a normalised distance of 0.003. The essential feature of our FE studies is that at this distance an unambiguous matching of the principal stress after WPS could not be obtained by matching to the critical stress for onset of fracture in as-received condition. This was irrespective of the material hardening model used in the FE analysis. These findings suggest that the stress superposition approach developed by Curry [16] and extended by Smith and Garwood [17] is not an appropriate model.

In contrast, when matching of the maximum principal stresses for the as-received and WPS cases is extended for larger distances ahead of the crack tip (and outside of the plastic zone developed in each case) FE predictions of the WPS fracture load (and stress intensity factor) are very similar to the displacement superposition model developed by Chell [2] at low pre-load levels. In Chell's model the J -integral is shrunk onto the yielded region and contains only the elastic displacements when the reloading plastic zone is within the overload plastic zone. The elastic displacements in this region arise from stress field developed outside of the plastic zones.

The stress matching method developed here also suggests that if an analytical method is to be developed, other than the displacement superposition method developed by Chell, then terms other than the singular HRR field are required. For example, it is evident that the pre-loading and unloading introduces a compressive residual stress field ahead of the crack tip that extends ahead of the crack tip to about 2% of the uncracked ligament (as shown in Fig. 5). On reloading at the lower temperature the stress field interacts with these residual stresses. Close to the crack tip the onset of plasticity during re-loading effectively diminishes the presence of the residual stresses. However, further away there is only elastic superposition of the compressive residual and the tensile applied stress. This in turn provides an enhancement and increases the load at fracture after WPS that is greater than the as-received fracture load.

When reloading after WPS the near crack tip residual stresses are redistributed due to plasticity created during reloading. Consequently, the details of the material hardening model close to the crack tip appear to be unimportant even though very different residual stress fields are developed near to the crack tip for each hardening model as shown in Figs. 4 and 5. Furthermore, at larger distances from the crack tip the residual stress following WPS arises from elastic recovery alone and is not influenced by the hardening model. For example this can be seen in Fig. 5 for normalised distances greater than 0.006.

The results of the FE analysis presented here indicate that the presence of the residual stresses generated by proof loading is the main reason for the enhancement in the toughness compared with the as-received toughness. The excellent agreement between the FE results and the Chell model at low levels of proof loading for sharp, blunted and extended cracks after proof loading also reinforces the argument that the residual stresses are the main underlying feature of the WPS effect. This is examined further in the next part of the discussion.

5.2. Application of FE results to experimental results

In paper 1 the displacement superposition model (by Chell) was combined with a failure probability model [5] to predict the influence of WPS on the fracture failure probability. In general the predicted failure probabilities were greater (more conservative) than the experimental results. This is illustrated in Fig. 10 where experimental results for tests using A533B steel at -170 and -100 $^{\circ}\text{C}$. At -170 $^{\circ}\text{C}$ there was a predicted improvement in toughness similar to the experiments, while at -100 $^{\circ}\text{C}$, the model predicted no

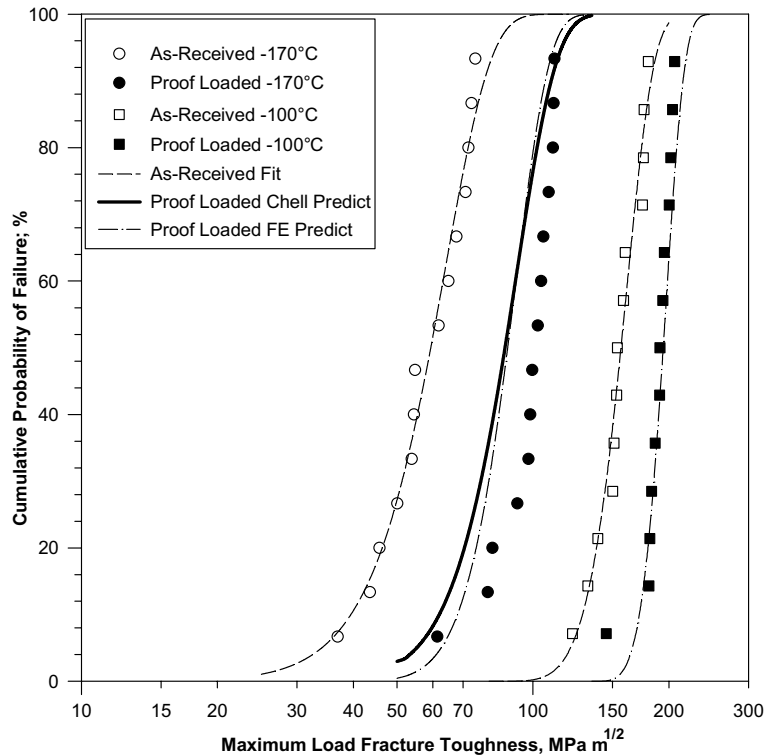


Fig. 10. Comparison of FE and Chell predictions of probability distribution of fracture toughness following WPS for A533B steel 50 mm thick SEN(B) specimens.

improvement in toughness. This was contrary to the experimental evidence shown in Fig. 10. Similar findings were obtained for BS1501, where in general the predicted failure probability after WPS was higher than observed in the experiments.

The results of the FE analysis revealed that the predicted toughness after WPS (and noting that the predictions were made assuming stress matching) was greater than predicted by Chell's [2–4] displacement superposition model. The predicted increase in toughness following proof loading using the FE analysis, shown in Fig. 6, was used in the combined probability of failure and WPS model developed in paper 1. The results of the predictions of this model are shown in Fig. 10. There is a small change in the prediction compared with the Chell model at the lower temperature ($-170\text{ }^{\circ}\text{C}$), but notably at the high fracture temperature ($-100\text{ }^{\circ}\text{C}$) an improvement in toughness is predicted whereas the Chell model predicts no change in toughness. The increased improvement in toughness predicted from the FE is also consistent with the results from earlier studies summarised in Fig. 1, where the experiments at high pre-loads lie above the predictions from Chell's model.

Assuming that cleavage fracture is characterised by the distribution of the maximum principal stress directly ahead of the crack tip, the results from the FE analysis have shown that the contributing factor to the benefit provided by WPS is the residual stress. Furthermore, the residual stresses that contribute to the improvement are not those directly at the crack tip, but those at some distance outside of the dominant HRR field. These results together with the comprehensive results presented in paper 1 suggest that neither crack tip blunting nor strain hardening plays an important role in the improvement in toughness following warm pre-stress.

6. Conclusions

Finite element analysis, combined with matching of the characteristic maximum principal stress distribution at fracture in the as-received state, has predicted the fracture load after warm pre-stressing. Fracture after WPS was predicted for sharp, blunt and extended cracks.

There is good agreement between the finite element results and the displacement superposition model developed by Chell. It is also demonstrated that using a simple model with a critical stress located at a characteristic distance for predicting the influence of WPS is not sufficient.

The sole contributing factor that provides the improvement in toughness after WPS is shown to be the residual stresses generated after proof loading. This is confirmed by comparing the results from the FE analysis with the experimental results presented in paper 1.

Acknowledgements

This work was supported by EPSRC grants GR/J10785 and GR/N10714, and in collaboration with TWI Ltd., British Energy, the Health and Safety Executive, Rolls-Royce and Power Engineering Plc. We would like to particularly thank Steve Garwood and Keith Bell, both formerly at TWI and Amin Mohammed (still at TWI) for their support and advice during this work. Saeid Hadidimoud would like to thank Ferdowsi University of Mashhad, Iran for granting him permission to participate in this work.

References

- [1] Smith DJ, Hadidimoud S, Fowler H. The Effects of Warm Pre-Stressing on Cleavage Fracture. Part 1: Evaluation of Experiments, companion paper.
- [2] Chell GG, Haigh JR, Vitek V. A theory of warm pre-stressing: experimental validation and the implications for elastic plastic failure criteria. *Int J Fract* 1981;17(1):61–81.
- [3] Chell GG. Some fracture mechanics applications of warm pre-stressing to pressure vessels. In: Proceedings of 4th International Conference Pressure Vessels Technology, IMechE, 1980. p. 117–24.
- [4] Chell GG, Haigh JR. The effect of warm pre-stressing on proof tested pressure vessels. *Int J Pres Ves Pip* 1986;23:121–32.
- [5] Wallin K. Statistical modelling of fracture in the ductile-to-brittle transition region. In: Blauel JG, Schwalbe KH, editors. Defect Assessment in Components, Fundamentals and Applications, ESIS/EGF 9. London: Mechanical Engineering Publications; 1991. p. 415–45.
- [6] Smith DJ, Garwood SJ. The significance of prior overload on fracture resistance: A critical review. *Int J Press Ves Pip* 1990;41:255–96.
- [7] Smith DJ, Garwood SJ. Application of theoretical methods to predict overload effects on fracture toughness of A533B steel. *Int J Pres Ves Pip* 1990;41:333–57.
- [8] Burdekin FM, Lidbury DPG. Views of TAGSI on the current position with regard to benefits of warm pre-stressing. *Int J Pres Ves Pip* 1999;76:885–90.
- [9] Beremin FM. A local criterion for cleavage fracture of a nuclear pressure vessel steel. *J Metall Trans A* 1983;14A:2277–87.
- [10] Stöckl H, Bösch R, Schmitt W, Varfolomeyev I, Chen JH. Quantification of the warm pre-stressing effect in a shape welded 10 MnMoNi 5-5 material. *Engng Fract Mech* 2000;67(2):119–37.
- [11] Kordisch H, Bösch R, Blauel JG, Schmitt W, Nagel G. Experimental and numerical investigations of the warm pre-stressing (WPS) effect considering different load paths. *Nucl Engng Des* 2000;198:89–96.
- [12] Valeta MP, Sainte Catherine C, Barbier G, Lefevre W, Eisele U, Bhandari S. Structural behaviour during a PTS transient taking into account the WPS effect. *Int J Pres Ves Pip* 2001;78:137–46.
- [13] Yagawa G, Yoshimura S, Soneda N, Hirano M. Probabilistic fracture mechanics analyses of nuclear pressure vessels under PTS events. *Nucl Engng Des* 1997;174:91–100.
- [14] Lidbury DPG, Bass BR, Bhandari S, Sherry AH. Key features arising from structural analysis of the NESC-1 PTS benchmark experiment. *Int J Pres Ves Pip* 2001;78:225–36.
- [15] Chen JH, Wang VB, Wang GZ, Chen X. Mechanism of effects of warm pre-stressing on apparent toughness of precracked specimens of HSLA steels. *Engng Fract Mech* 2001;68(2):1669–86.

- [16] Curry DA. A micro-mechanistic approach to the warm pre-stressing of ferritic steels. *Int J Fract* 1981;17(3):335–43.
- [17] Smith DJ, Garwood SJ. The Application of Fracture Mechanics to Assess the Significance of Proof Loading. In: Ernst HA, Saxena A, McDowell L, editors. *Fracture Mechanics: 22nd Symposium ASTM STP 1131*, Philadelphia, vol. 1, 1992. p. 833–49.
- [18] Smith DJ, Garwood SJ. Experimental study of effects of prior overload on fracture toughness of A533B steel. *Int J Pres Ves Pip* 1990;41:297–331.
- [19] Bilby BA, Cotterell AH, Swinden KH. The spread of plastic yield from a notch. *Proc Roy Soc A* 1963;272:304–14.
- [20] Ritchie RO, Knott JF, Rice JR. On the relationship between critical tensile stress and fracture toughness in mild steel. *J Mech Phys Solids* 1973;21:395–410.
- [21] Hutchinson JW. Singular behaviour at the end of a tensile crack in a hardening material. *J Mech Phys Solids* 1968;16:13–31.
- [22] Rice JR, Rosengren GF. Plane strain deformation near a crack tip in a power law hardening material. *J Mech Phys Solids* 1968;16:1–12.
- [23] Reed PAS, Knott JF. An investigation of the warm pre-stressing (WPS) effect in A533B weld metal. *Fatigue Fract Engng Mater Struct* 1992;15(12):1251–70.
- [24] Reed PAS, Knott JF. Investigation of the role of residual stress in the warm pre-stress (WPS) effect part I—experimental. *Fatigue Fract Engng Mater Struct* 1996;19(4):485–500.
- [25] Reed PAS, Knott JF. Investigation of the role of residual stress in the warm pre-stress (WPS) effect part II—analysis. *Fatigue Fract Engng Mater Struct* 1996;19(4):501–13.
- [26] Loss FJ, Gray Jr RA, Hawthorne JR. Significance of warm pre-stress to crack initiation during thermal shock. *Nucl Engng Des* 1978;46:395–408.
- [27] Fowler H, Smith DJ, Bell K. Scatter in cleavage fracture toughness following proof loading. In: *Advances in fracture research. Proceedings of 9th International Conference Fracture (ICF 9)*, vol. 5, 1997. p. 2519–26.
- [28] Fowler H. PhD Thesis: The influence of warm pre-stressing and proof loading on the cleavage fracture toughness of ferritic steels. University of Bristol, 1998.
- [29] Hibbit, Karlsson, Sorensen, Inc., ABAQUS/CAE, Version 6.2, 2001.